Fractal Nature of Viscous Fingering in Two-Dimensional Pore Level Models

M. Ferer, W. Neal Sams, R. A. Geisbrecht, and Duane H. Smith
Morgantown Energy Technology Center, Morgantown, WV 26507

Use of saturation-dependent relative mobilities leads to linear flow; however, experiment and theory show that, in the limit of very large viscosity ratio, the flow is not linear but fractal. Generally, fractional flows and relative mobilities depend on both saturation and time. Use of a standard pore-level model of 2-D flow in the limit of infinite capillary number shows that this flow is fractal for large viscosity ratios ($M = 10{,}000$) and the saturation and fractional flows agree with the results of our general arguments. For realistic viscosities ($M = 3 \rightarrow 300$), our modeling of the unstable flow shows that, although the flows are initially fractal, they become linear on a time scale, τ, increasing as $\tau = \tau_0 M^{0.17}$. Once linear, the saturation front advances as $x \approx v_0 M^{0.068} t$; the factor $M^{0.068}$ acts as a 2-D Koval factor.

Introduction

Composition-dependent relative mobilities are used in all traditional modeling of flow in porous media, such as Buckley-Leverett or Koval (Collins, 1961; Rhee et al., 1986). Their use predicts flow in which the saturation front advances linearly with time. However, it has been shown that the limit of infinite viscosity ratio ($M \rightarrow \infty$, where the injected fluid has zero viscosity) is accurately described by diffusion-limited aggregation (DLA), a process that is known to form fractal objects with nonuniform densities (Vicsek, 1989; Witten and Sander, 1981; Meakin, 1983a). For fractal flow, the saturation front advances faster than linearly with time. Two questions naturally arise: (1) If the actual viscous fingering were fractal, what would be the effect on traditional simulation? and (2) Is the viscous fingering fractal for realistic, unstable viscosity ratios? As we will see, our modeling indicates that large-scale flows are not fractal, but that small-scale flows are fractal. Furthermore, this crossover from small-scale fractal flows to large-scale linear flows leads to definite predictions regarding the dependence of flow velocity upon viscosity ratio.

First, what is a fractal? The classic signature of a fractal object is a non-Euclidean relationship between mass and size. If one has an ordinary solid disk, the mass is proportional to R^2, but for a circular fractal object, the mass is proportional to R^{D_f}, with a noninteger fractal dimension, D_f; for example, for DLA, $D_f \approx 1.7$. Therefore, a fractal object is less dense than an ordinary object due to material voids inside the object. However, it should be emphasized that neither the mass density nor the compensating voids are uniformly distributed; indeed, the mass density decreases with R while the void density must increase with R. Formation of these fractals is an unstable, nonequilibrium process. A number of excellent reviews discuss a wide variety of these fractal growth phenomena, including material deposition, dielectric breakdown, and two-phase flow in porous media, the topic of this article (Vicsek, 1989; Mandelbrot, 1982; Feder, 1988).

Second, what is viscous fingering? If the flow is "unstable" (viscosity ratio $M > 1$), the injected fluid fingers into the displaced fluid (Saffman and Taylor, 1958). This effect has been widely studied in "Hele-Shaw" cells, where a high viscosity fluid occupies the space between two flat glass plates, and a low-viscosity fluid is injected at the center. If the viscosity ratio is large enough, the viscous fingering patterns satisfy a fractal relationship with fractal dimension $D_f = 1.70 \pm 0.05$ (Daccord et al., 1986). If the space between the Hele-Shaw plates is filled with a bead pack, mimicking a porous medium, analysis of the fingering for large viscosity ratio (air into epoxy) results in a fractal dimension of $D_f = 1.62 \pm 0.04$ (Maloy et al., 1985).

In the growth of fractal DLA patterns, the patterns initially have many small fingers, some of which grow faster than others. The longer fingers grow more rapidly than the short

Correspondence concerning this article should be addressed to M. Ferer at his permanent address, Physics Dept., Box 6315, W. Va. Univ., Morgantown, WV 26506.

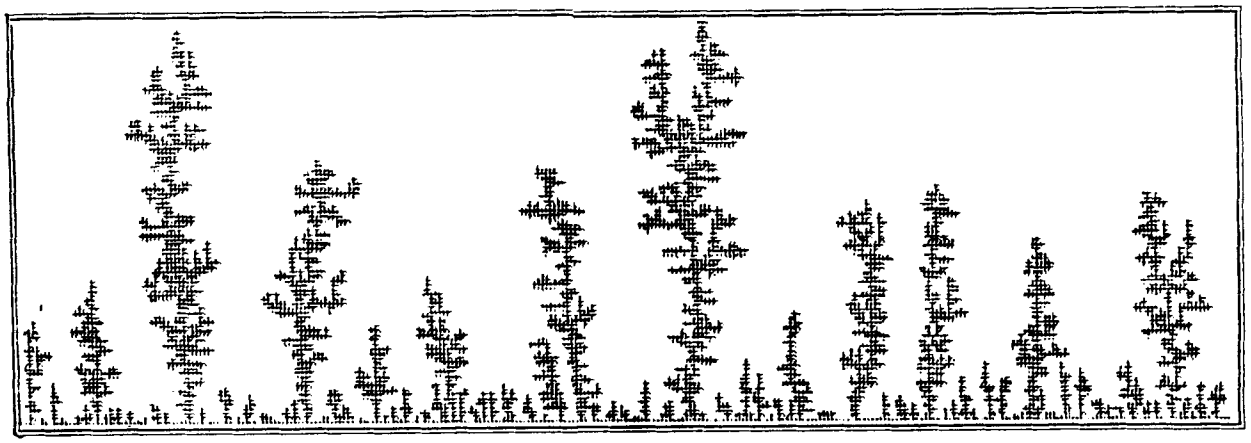

Figure 1. Near-breakthrough flow pattern in pore bodies and throats.

They are occupied by injected fluid for a 90×300 porous medium resulting from our simulations with a fluid viscosity-ratio $M = 10{,}000$.

fingers, so that as the object grows it "coarsens" (it has fewer and fewer growing fingers) (Meakin, 1983b). Therefore, at an advanced stage of growth the pattern has fingers on many different size scales, giving a nonuniform density (or saturation) profile (see Figure 1). If these fractal flows dominate viscous fingering for realistic, unstable viscosity ratios, then the saturations will not be uniform and *neither fractional flows nor relative permeabilities will depend simply upon saturation as is universally believed*; this conclusion is shown in detail in the following section.

It is tempting to interpret the numerous experimental results, for example, from core floods, as verifying that relative permeabilities do simply depend upon uniform saturations of injected fluid (Blackwell et al., 1959). However, the large aspect ratio (long-narrow geometry) of experimental cores makes even fractal DLA-like flow appear nonfractal. As a fractal DLA pattern grows in the confines of a long-narrow geometry, eventually only one growing finger remains from "the fewer and fewer growing fingers." Therefore, the increased amount of the injected fluid in the core all goes into increasing the length of this one dominant finger, which then grows linearly with the amount of injected fluid (Nittmann et al., 1985). Thus, after the initial stage of flow in a long-narrow core, the front between the injected and the displaced fluids (tip of the single dominant finger) advances linearly with time (total saturation or amount of injected fluid). This pseudolinear flow is imposed by the artificial geometry of the measurement. For DLA-like flow in a short-wide system, no single finger is dominant (Figure 1) (Nittmann, 1985; Meakin, 1983b); and the average position of the saturation, $\langle x \rangle$ (related to the location of the front) has a nonlinear power-law dependence upon the total saturation or time, t:

$$\langle x \rangle = Ct^{1+\epsilon}, \tag{1}$$

where

$$1 + \epsilon = 1/(D_f - 1).$$

For two-dimensional, DLA-like flow, $D_f \approx 1.7$ and $\epsilon \approx 0.4$ (for three-dimensions, $D_f \approx 2.5$ and $1 + \epsilon \approx 2$) (Meakin, 1983a; Vicsek, 1989; Nittmann et al., 1985). Therefore, the dependence of relative permeability upon uniform saturation in core floods may simply be an artifact of the large aspect ratio of these systems. The validity of the assumption of the nonfractal dependence of relative permeabilities on uniform saturation is still an open question.

In the following section we address the question: What effect would fractal viscous fingering have upon saturation profiles and fractional flow curves? For fractal flow, we determine the functional forms of saturation profile, $S(x)$, and fractional flow, $F(x)$, curves, where $S(x)$ is the linear density of injected fluid and $F(x)$ is the ratio of injected fluid flow to total flow past position x. These fractal forms are significantly different from traditional forms; in particular, the fractional flow is a function not of the saturation S but rather of $t^{\epsilon}S$. The "scaling" arguments used to derive the expressions for saturation and fractional flow are very similar to those used in a wide range of fields including critical phenomena (Fisher, 1967; Kadanoff et al., 1967), coalescence phenomena (Tobin et al., 1990), polymer physics (de Gennes, 1979), aggregation phenomena (van Dongen and Ernst, 1984, 1985), and percolation theory (Stauffer, 1985). For those readers who are not familiar with these scaling arguments, a detailed derivation of these forms is presented in Appendix A. We then discuss our modeling of two-phase flow in two-dimensional porous media and present results that show that (1) the flow is unambiguously fractal for a large viscosity ratio, $M = 10{,}000$, and (2) the results for saturation profile and fractional flow, from this fractal model, agree with our predicted functional dependencies.

In modeling unstable two-phase flow in porous media, we have used one of the most standard and most physically rigorous models possible. Variants of this model have been widely used to study various aspects of the flow in porous media (Chen and Wilkinson, 1985; Lenormand et al., 1988; Siddiqui and Sahimi, 1990; King, 1987). This work verified that the flows were fractal for large viscosity ratios and that the flows were linear (or compact) for small viscosity ratios, which is consistent with our quantitative characterization of a crossover from small-scale fractal flow to large-scale linear/compact flows. For those readers not familiar with

these models from previous work, a detailed discussion is presented in Appendix B. Our studies used a standard square-lattice model of homogeneous two-dimensional porous media (Fatt, 1956; Lenormand et al., 1988; Chen and Wilkinson, 1985) in which the pore bodies at the sites of a square lattice all have unit volume, but the cross-sectional area of each pore throat is randomly chosen from a uniform distribution, which is known to give random, fractal flow for infinite viscosity-ratio (Chen and Wilkinson, 1985). To model flow in the limit of infinite capillary number, we used Poiseuille's law to determine the conductances (or transmissibilities) from the geometry and the location of the interface; we then use a slight modification of the standard Gauss-Seidel iteration (Peaceman, 1977) of the discrete Laplace equation to determine the pressure field. Since we know that the pressure drops across the throats and the conductances, Poiseuille's law enables us to determine the flow rate for each throat. We then use a straightforward deterministic procedure to advance the interface through a short time Δt. Flow is allowed in every throat, and the deterministic flow velocity is allowed to advance or retreat the interface within the pore throat, into its connecting pore body, and through a pore body into its outflow throats. Our simulations of flow for this model satisfy total fluid conservation to within 0.5 percent, even after 1,400 time steps. This procedure has the advantage of not suppressing fractal flow (Lenormand et al., 1988), as do averaged methods like the grid-block procedures (Thomas, 1982); indeed, earlier variants of this model were used to study fractal flow (Lenormand et al., 1988; Chen and Wilkinson, 1985; Thomas, 1982). As discussed in the following section, the large viscosity-ratio limit of this model does produce the expected DLA-like fractal flows.

We addressed the question, "Is viscous fingering fractal for realistic viscosity-ratios?" Using the model discussed earlier and detailed in Appendix B, we study the time dependence of the first moment, that is, $\langle x(t)\rangle$, for viscosity ratios $M = 3$ to 300. For these viscosity ratios and probably for all finite viscosity ratios, the simulations produce initial fractal flows obeying Eq. 1 that become compact (or linear),

$$\langle x\rangle = vt, \tag{2}$$

on a characteristic time scale that increases with viscosity ratio. It is shown that the fractal-to-compact "crossover" can be convincingly fit by a simple exponential approach to a constant $\langle x\rangle/t = v$. Although the output of the fitting procedure has too much error to accurately determine the viscosity-ratio dependence of the characteristic time τ and the "front" velocity v, such a determination is possible from a collapse of the $\langle x\rangle$ vs. t data for all viscosity ratios onto a single curve. Our assumption of negligible dispersion should be a worst-possible-case scenario for fractal-to-compact crossover in the limit of infinite capillary number, because dispersion will smooth the interface, thereby favoring compact flow and accelerating the fractal-to-compact crossover. Extending the functional forms of the saturation profile and fractional flow of the next section to include finite viscosity ratios enables us to determine a two-dimensional "Koval"-like factor in the postcrossover, compact-flow regime (Koval, 1963). This extension of fractal scaling agrees with results of our simulations for the postcrossover dependence of fractional flow upon saturation and the viscosity ratio.

Effects of Fractal Viscous Fingering on Saturations and Fractional Flows

Traditional modeling uses composition-dependent relative mobilities. From such composition-dependent relative mobilities, it is straightforward to show that the saturation front advances linearly with time so that the first moment of the saturation also increases linearly with time, $\langle x\rangle = vt$ (Eq. 2). Conventional usage defines the total saturation, $S_{\text{tot}} = \int_{x=0}^{L} S(x, t)\, dx$, to be the percent of total volume occupied by the injected fluid at time t, and $F(x, t)$, which is the fraction of total fluid flow past point x, is the current for the linear density $S(x, t)$. Furthermore, the saturation and fractional-flow profiles scale with x/t, that is, $S(x, t) = \zeta(x/t)$ and $F(x, t) = f(x/t)$. Thus, the variable x/t can be determined by inverting the saturation, S, that is, $x/t = \zeta^{-1}(S)$; consistent with the initial assumptions the fractional flow is a function of saturation $F(S) = f(\zeta^{-1}(S))$ (Collins, 1961; Thomas, 1982; Buckley and Leverett, 1942). Thus, the usual saturation dependence of the fractional flow goes hand-in-hand with the linear relationship between front location and time. If the flow is fractal, the first moment of the saturation advances faster than linearly with time, $\langle x\rangle = Ct^{1+\epsilon}$ (Eq. 1) (Meakin, 1983b; Vicsek, 1989), and the profiles of saturation and fractional flow no longer depend solely upon x/t. The functional forms of saturation, S, and fractional flow, F, which are consistent with Eq. 1 for the advance of fractal flow,

$$S(x, t) = t^{-\epsilon} s(x/t^{1+\epsilon}), \tag{3}$$

and

$$F_f = F(t^{\epsilon} S), \tag{4}$$

follow from Eq. 1 (Meakin, 1983b) using standard "scaling" arguments (Kadanoff et al., 1967; Fisher, 1967; de Gennes, 1979; van Dongen and Ernst, 1984; Tobin et al., 1990; Stauffer, 1985) as detailed in Appendix A. Equation 3 shows that the saturation depends upon $x/t^{1+\epsilon}$. The multiplicative factor of $t^{-\epsilon}$ arises because the total saturation is proportional to the time (assuming a constant injection rate); and, indeed, serves as a definition of time. Physically the factor of $t^{-\epsilon}$ indicates that as the front advances, the saturation at the front decreases because there are fewer and fewer fingers and less and less injected fluid at the front. Therefore, it is a general result for fractal flow that the fractional flow depends not simply upon saturation S but also on time through the variable $t^{\epsilon}S$, where the factor of t^{ϵ} scales up the decreasing saturation at the front.

Next, we show that our modeling produces fractal flow for a large viscosity ratio, enabling us to check the predictions in Eqs. 3 and 4. Using a viscosity ratio of 10,000, we ran our modeling program up to breakthrough for 17 different realizations of our model porous medium, all of which were $N_y = 300$ pore bodies wide. Each of these realizations was generated by starting with a different seed for the random number generator on our floating-point systems (FPS) machine. Of these 17 realizations, 11 were $N_x = 60$ pore bodies long and

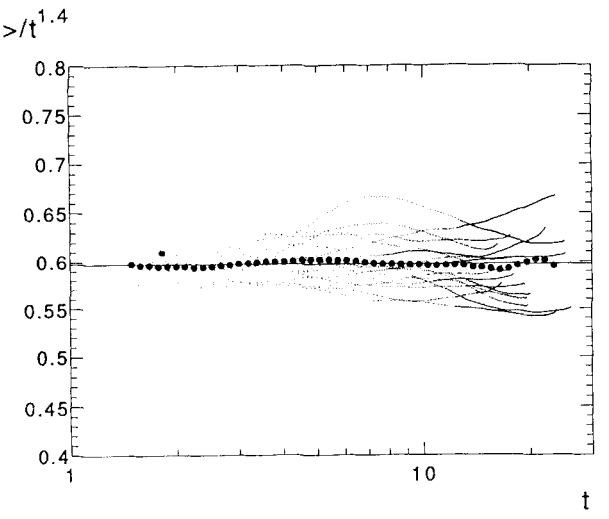

Figure 2. Fractal behavior of the average position ($\langle x \rangle = Ct^{1.4}$) from modeling large viscosity-ratio flows with $M = 10{,}000$ on 17 different realizations of the porous medium.

· · · track the flow for individual realizations; ●●● result from the data-smoothing procedure.

six were $N_x = 90$ pore bodies long. Two additional realizations of larger systems $N_x = 96$ pore bodies long by $N_y = 640$ pore bodies wide were performed on a CRAY YMP. Figure 1 shows a typical, near-breakthrough pattern for one of the 90×360 porous media; this pattern does appear to be fractal, having fingers of many different sizes looking very much like the patterns from on-lattice DLA simulations (Vicsek, 1989; Meakin, 1983b). We purposely chose to model the flow on short-wide systems to avoid the pseudolinear flow produced in long-narrow systems by the dominance of one single finger.

During each of these runs, we have determined the time (mass of injected fluid) and $\langle x \rangle$ (average position of injected fluid) at each time step. Furthermore (at specific values of t), we have determined the saturation profile $S(x, t)$ by finding the fraction of the total volume available in the $x = 2i$ row of pore bodies and pore throats (that is, the throats in the row $x = 2i$ plus those in the row $x = 2i - 1$) that is occupied by injected fluid; and we have determined the fractional flow profile $F(x, t)$ by integrating (summing) the rate of change of $S(x, t)$ over positions from 0 to $x(2i)$ since

$$\frac{\partial F(x, t)}{\partial x} = -\frac{\partial S(x, t)}{\partial t}.$$

In order to verify that our model with this large a viscosity ratio ($M = 10{,}000$) is producing fractal flow, we have studied the dependence of $\langle x \rangle$ upon t. Figure 2 shows the log-log plot of $\langle x \rangle / t^{1.4}$ vs. t. Our specific definition of t is proportional to the total volume of injected fluid V_{tot}, which is also proportional to the total saturation, through the relation

$$t = 1.2 + (V_{\text{tot}}/N_y). \tag{5}$$

For this linear flow problem, where low viscosity fluid is injected into all the N_y inlet pore bodies along the width, the factor of N_y in Eq. 5 accounts for the width dependence of the injection rate, allowing us to compare systems of different widths used in some of the later simulations. The additive factor of 1.2 shifts the time origin, and serves to remove the early time curvature in Figure 2; its effect at later times is insignificant. This time shift is similar in spirit to a shift in the location of $x = 0$ used in earlier DLA work to remove early time (short-distance) curvature (Meakin, 1983b). It is interesting that the factor of 1.2 is just the time shift that arises when one relates the sums in our discrete model to the integrals in more physical continuous systems; this relationship is derived in Appendix C. If the flow is a DLA-like fractal, $\langle x \rangle / t^{1.4}$ will be constant for all t. The points track the results from runs on individual, porous media realizations. Finite-size effects seem negligible in the near-breakthrough data, since results for the smaller systems near breakthrough (near $t \approx 17$, the 60×300 models reach breakthrough) are statistically indistinguishable from results for the larger systems (90×300), well before breakthrough. This lack of finite size effects has been verified for all viscosity ratios, more convincingly so for some of the other values where we have simulations for a greater range of lengths and breakthrough times. The solid circles show the results of a data-smoothing procedure in which we performed a quadratic least-squares fit of all the data ($y = \ln(\langle x \rangle / t)$, $x = \ln t$), with $x = \ln t$ in the interval ($\ln t_i - \frac{1}{4}$, $\ln t_i + \frac{1}{4}$). This gives the location of the ith solid circle ($(\langle x \rangle / t)_i$, t_i) and its standard error. We then let $\ln t_i$ scan the full range of the data. The standard errors are no bigger than the solid circles used in Figure 2. The first moment does, indeed, show fractal scaling $\langle x \rangle \propto t^{1.4}$, which from Eq. 1 is consistent with the DLA value of the fractal dimension, $D_f \approx 1.7$. To estimate our certainty in the value of 1.4, we plotted $\langle x \rangle / t^{1.45}$ and $\langle x \rangle / t^{1.35}$; on the scale of Figure 2, these were clearly tilted from the horizontal. Therefore, we estimate $1 + \epsilon = 1.40 \pm 0.05$ and $D_f = 1.71 \pm 0.3$; these results from our model are in good agreement with the on-lattice DLA fractal dimension (Meakin, 1983a).

Having demonstrated the {DLA-like} fractal nature of our model, we then averaged the saturation and fractional flow profiles of the 17 different systems on which simulations were performed. These results are shown in Figures 3 and 4 for the times $t = 5$, 9, and 15. For these figures, we have used a definition of time that is the standard % saturation for the shorter systems that are 60 pore bodies long, so that $t = \{100\%\} \times \{1.2 + (V_{\text{tot}}/N_y)\}/(2 \times 60)$; the factor of 2 arises from the presence of two unit volumes per pore body (one inside each pore body and the second inside each average pair of pore throats). Figure 3 shows saturation profiles for these three times. In Figure 3a, one sees the time evolution of the saturation profiles; characteristic of fractal flow, there is very little change for the small x saturations, since most of the fractal "growth" is occurring at the fingertips. Figure 3b shows the attempt to represent these profiles as a function of x/t, as in the traditional linear theory; to within many standard errors, there is no tendency for the curves to overlap. On the other hand, Figure 3c shows how well our modeling results agree with the functional form predicted in Eq. 3; the small deviations occurring in the $t = 5$ data are short-time (transient) corrections to asymptotic scaling. Figure 4a shows the

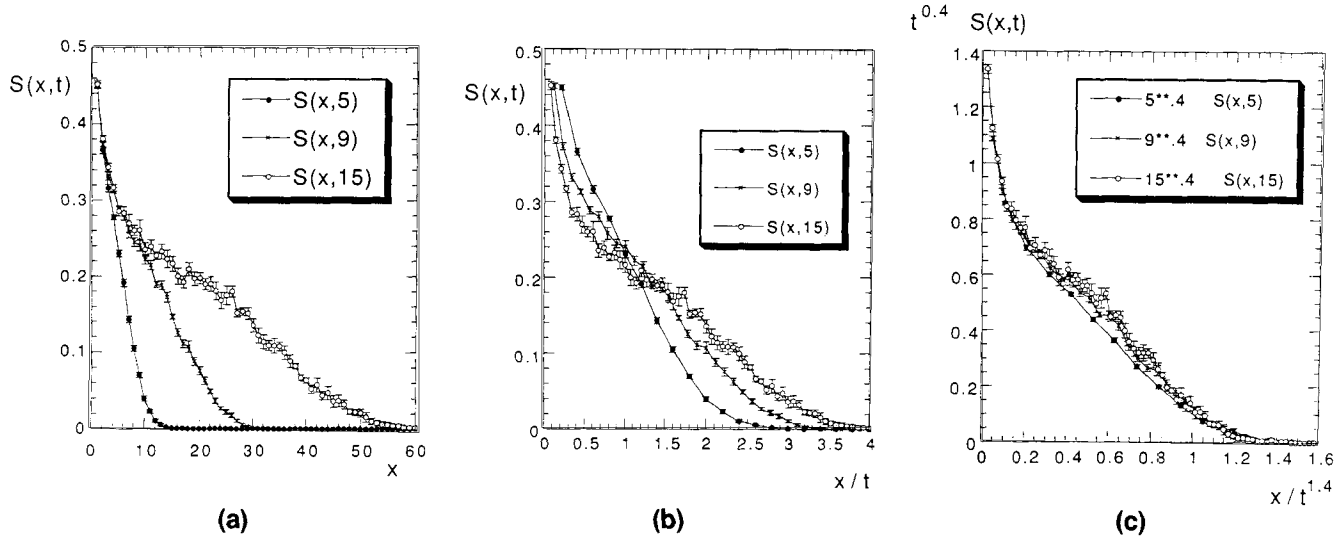

Figure 3. Saturation from flow with $M = 10{,}000$ at three times: $t = 5$, 9, and 15.

(a) Relative constancy of small-x saturations (consistent with the observation that the majority of the fractal flow occurs near the tips of the viscous fingers); (b) test of the linear flow prediction of $S(x, t)$ as a function of x/t (violations of this linear flow prediction exceed several standard errors); (c) test of fractal predictions for saturation profile $S(x, t) = S(x, t) = t^{-\epsilon}s(x/t^{1+\epsilon})$ (agreement with Eq. 3 is excellent).

fractional flow vs. saturation for the same three times; again contrary to the traditional model, the curves fail to overlap by several standard deviations, with a clear trend toward larger fractional flows for lower saturations as time increases. This trend is correctly described by the fractal "scaling" expression in Eq. 4, as shown in Figure 4b where the fractional flows at the three times are represented by the same function $F(t^{\epsilon}S)$ (they lie along the same curve) to within one standard deviation.

Summarizing, if the flow is fractal, traditional linear flow theory misrepresents the flow in significant, fundamental ways, as derived in general and as demonstrated for a specific

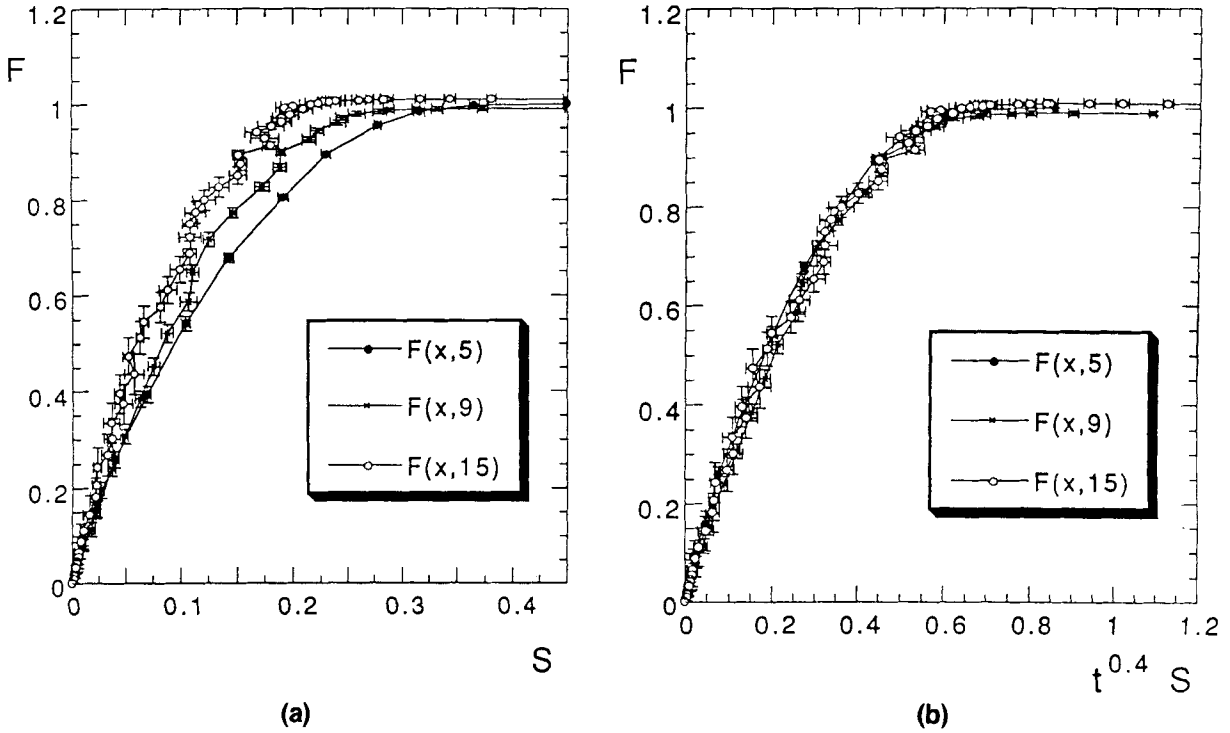

Figure 4. Fractional flow "curves" from flow with $M = 10^4$ at three times: $t = 5$, 9, 15.

(a) Standard fractional flow with clear dependence of fractal fractional flow on time with a trend toward larger fractional flows at lower saturations; (b) fractional flow vs. fractal "scaling" variable $t^{\epsilon}S$ (agreement with fractal "scaling" prediction in Eq. 4 is excellent with all the points lying along the same curve to within one standard error).

case of fractal flow from our model. Furthermore, since the fractional flow depends explicitly on saturation and time, the relative permeabilities must also depend explicitly on saturation and time. This effect was implicit in earlier work (Meakin, 1983b; Vicsek, 1989; Feder, 1988). We have attempted to make the consequences for saturation and fractional flow more explicit. Furthermore, at the end of the next section, we show that extensions of this "fractal scaling" make definite predictions regarding the viscosity ratio dependence of saturation and fractional flow.

Is Viscous Fingering Fractal for Realistic, Unstable Viscosity Ratios?

To study the nature of large-scale flows for finite viscosity ratios, we have modeled flows for realistic unstable viscosity ratios: $M = 3$, 10, 30, 100, and 300. For each viscosity ratio, we have used a number of different realizations of our model porous medium to improve statistics. Figure 5 shows the near-breakthrough flow pattern for three viscosity ratios; this figure demonstrates the previously observed tendency of large-viscosity-ratio flows to appear fractal while small-viscosity-ratio flows are visibly more compact (Lenormand et al., 1988). The extensive fragmentation of the interface, observed for viscosity ratios $M = 100$ and $M = 10$, results from fluctuations in the pressure gradient perpendicular to average flow. Without capillary pressure, very small pressure gradients can produce flow; thus it is not surprising that fluctuations in the pressure field lead to a sign change in the small pressure gradient, producing back flow that can pinch off fingers. This effect is nearly absent in radial flow where the fluctuations should be less significant (Ferer et al., 1992). To quantify the observed crossover from fractal flow to compact flow as a function of viscosity ratio and time, we have determined the average position of saturation, $\langle x \rangle$, and the time t, Eq. 5, at each time step in the simulations. Performing these simulations for a number of different realizations of the model porous medium, we smoothed the resulting data, as described earlier, for each viscosity ratio. Figure 6 shows the smoothed data for $\langle x \rangle / t$ vs. t for all the viscosity ratios studied; as before, the standard errors are no larger than the data points. As expected from our earlier discussion, the data for $M = 10{,}000$ show fractal behavior with $\langle x \rangle / t$ growing as $t^{0.4}$. For the smaller viscosity ratios, the curves first follow the fractal $t^{0.4}$ dependence; but, beginning with the $M = 3$ data, they all break away from the fractal behavior and approach a

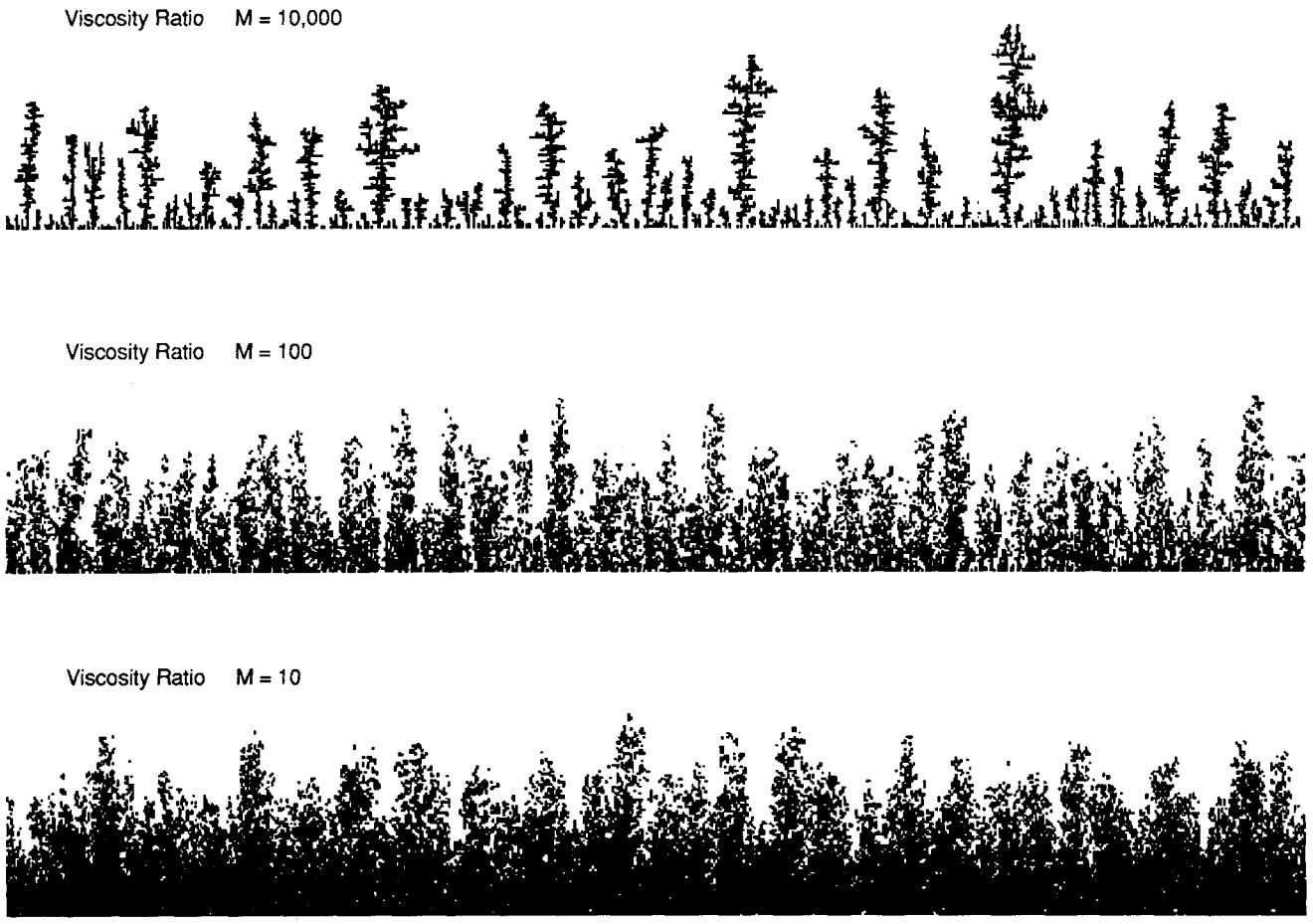

Figure 5. Near-breakthrough flow patterns in pore bodies occupied by injected fluid for three viscosity ratios, $M = 10^4$, 10^2, and 10.

These patterns are from simulations on our largest systems, which are 96 pore bodies long by 640 pore bodies wide. Note the apparent crossover from fractal to compact flow as the viscosity ratio decreases.

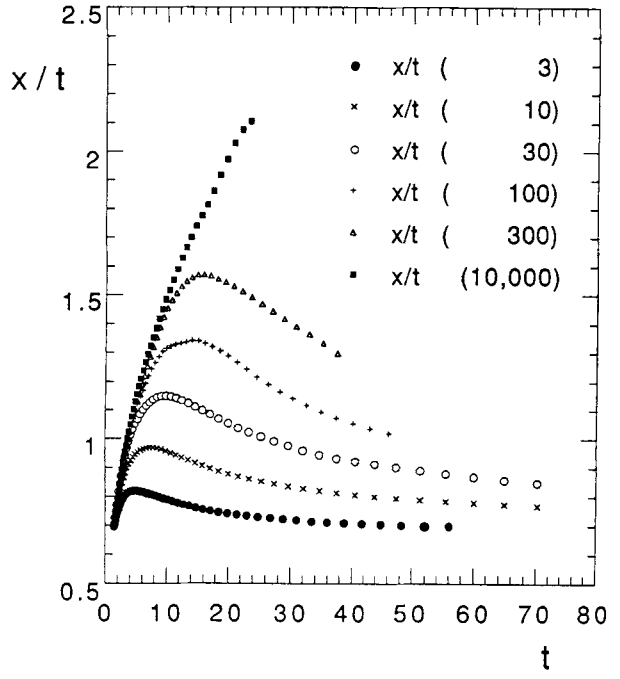

Figure 6. Smoothed data for $\langle x \rangle/t$ vs. t showing the crossover from initial fractal growth ($t^{0.4}$ behavior) to eventual compact growth ($\langle x \rangle/t = v$).

A characteristic time scale τ increases with viscosity ratio from $M = 3$ to $M = 10$, 30, 100, and 300, and eventually to $M = 10{,}000$, where the crossover has not yet begun.

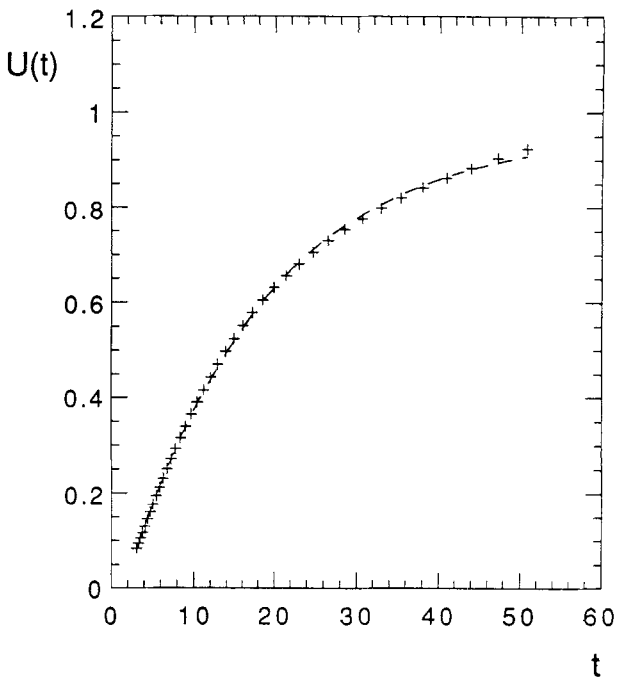

Figure 7. Remainder, as in Eq. 6, from the smoothed data for $M = 10$ and the best fit of this data to Eq. 7.

constant, $\langle x \rangle/t = v$, characteristic of compact (linear) flow. Furthermore, this breakaway or crossover occurs on a characteristic time scale, τ, which increases with viscosity ratio. In all cases, the flows follow the fractal behavior, overshoot, and then relax back to compact behavior. This intermediate, postovershoot flow has a decreasing $\langle x \rangle/t$, which indicates that the front ($\langle x \rangle$) is advancing more slowly than linearly with t so that the flow is denser than compact. Clearly this denser-than-compact (overdense) growth cannot be a long-term effect; however, it could represent a real, short-term filling of the voids formed during the fractal stage of growth. In any case, Figure 6 shows a well-defined crossover from initial fractal growth ($\langle x \rangle/t \approx t^{0.4}$) to eventual compact growth ($\langle x \rangle/t = v$) for all relevant viscosity ratios.

To quantify this process, it is necessary to determine the viscosity ratio dependence of the front velocity, $v(M)$, and characteristic crossover time, $\tau(M)$. It is natural to fit our smoothed data for $\langle x \rangle/t$. Unfortunately, we are hampered in not having strong candidates for a fitting function. One procedure that led to convincing fits started with the data for $t/\langle x \rangle$, the fractal part of which ($t^{-0.4}$) goes to zero for large times. Therefore, if we subtract the correct fractal part from our data for $t/\langle x \rangle$, we obtain

$$U(t) = (t/\langle x \rangle) - 1.678t^{-0.4}, \tag{6}$$

which contains all the information about the crossover to compact behavior where $U(t) \to v^{-1}$. For $M = 10$, this remainder, $U(t)$, is shown in Figure 7. The time dependence of the data resembles the time dependence of the potential across a charging capacitor as the potential exponentially approaches a constant:

$$U(t) = \frac{1}{v}(1 - e^{-(t+\Delta)/\tau}) \tag{7}$$

The parameter Δ represents a shift in the time scale, which was necessary to obtain good fits. For $M = 10$, the fit to this function is also shown in Figure 7, and the parameters determined from all the fits are given in Table 1. The values of the R factor from Table 1 show that this simple function provides a credible fit to our data. The large uncertainties in our values for τ and v do not allow a convincing determination of the viscosity-ratio dependence. However, as discussed below, a "scaling" argument does allow a convincing characterization of the viscosity-ratio dependence of τ and v.

In order to determine a "scaling" variable that will collapse all the data onto a single curve, consider the data for $\langle x \rangle/t^{1.4}$ shown in Figure 8. All the data start from a value of 0.596 =

Table 1. Estimates of the Front Velocity, v, and Characteristic Time, τ, from Fitting the Remainder, Eq. 6, from Our Finite Viscosity-Ratio Data to the Function in Eq. 7*

$M = \mu_D/\mu_I$	3	10	30	100
v	0.87 ± 0.04	0.97 ± 0.03	1.07 ± 0.03	1.1 ± 0.1
τ	20.0 ± 4.0	22.2 ± 4.0	27.0 ± 2.0	33.0 ± 5.0
R	0.9993	0.9998	0.9998	0.9997

*The goodness of fit (the R value) is gratifying, but the relatively small variations with M and the size of the errors preclude an accurate determination of the M-dependence from this approach.

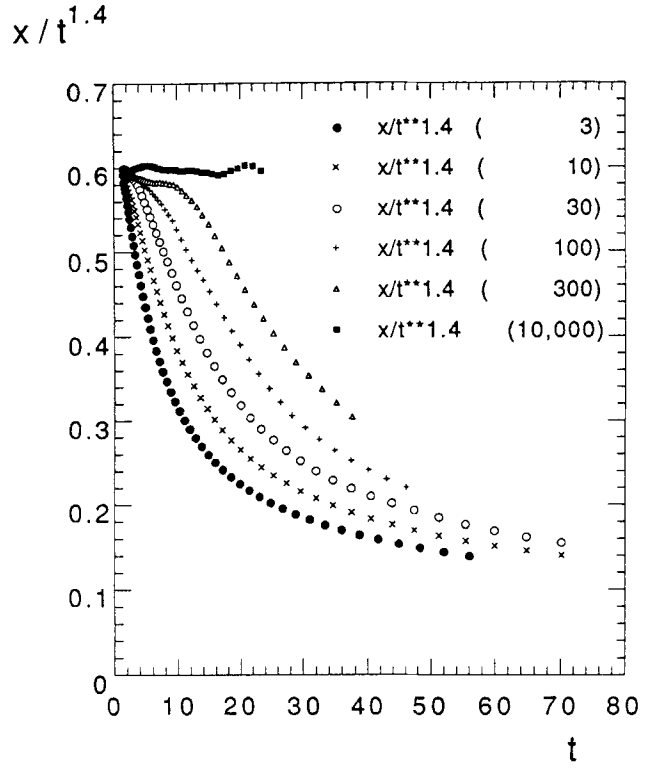

Figure 8. $\langle x \rangle / t^{1.4}$ vs. t from the smoothed data for all viscosity ratios.

The crossover from initial fractal behavior (constant) to eventual compact behavior ($t^{-0.4}$ dependence) on a characteristic time scale τ increases with viscosity ratio.

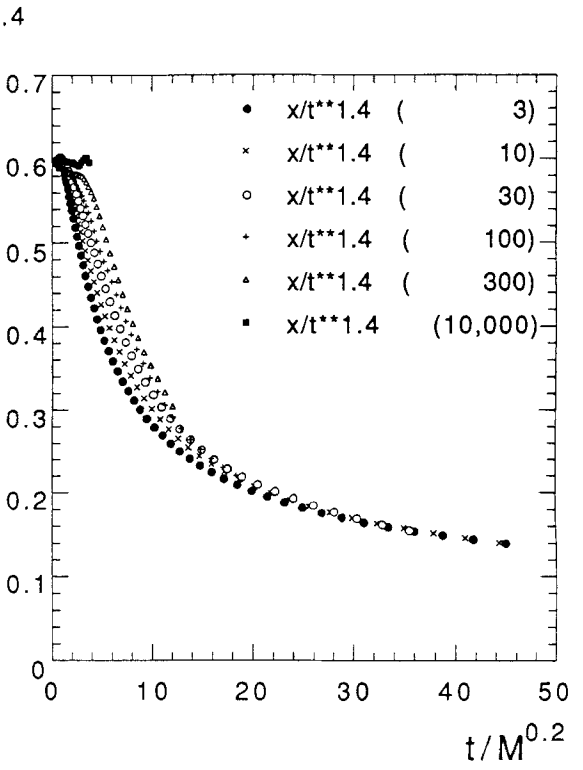

Figure 9. $\langle x \rangle / t^{1.4}$ vs. $t/M^{0.20}$.

A characteristic time increases with viscosity ratio as $\tau \propto M^{0.20}$ collapses the large-time data, with small deviations approximately $\Delta t \approx 5$ around $t \approx 10$.

1/1.678, characteristic of the fractal dependence, and eventually cross over to the compact behavior with a $t^{-0.4}$ dependence. One can obtain a crude collapse of the data by plotting the data vs. a scaling variable $t/M^{0.20}$, as shown in Figure 9, where the characteristic time factor, $M^{0.20}$, shifts the large viscosity-ratio data onto the smaller viscosity-ratio data. This estimate for the viscosity-ratio dependence of the relaxation time, that is, $\tau \approx \tau_0 M^{0.20}$, appears to provide convincing data collapse for large times, but not for the small time regime near $t \approx 10$, where there still remains a small viscosity-ratio-dependent spread of approximately $\Delta t \approx 5$ in the data. Recalling that a shift Δ of the time origin was needed to obtain convincing fits, as discussed earlier, we found that including a small viscosity-ratio-dependent time shift $\Delta = 8/M^{0.17}$ enabled us to obtain a much more convincing data collapse with the scaling variable $u = \{t + (8/M^{0.17})\}/M^{0.17}$, as shown in Figure 10. It should be noted that the index characterizing the relaxation time changed little from the value in Figure 9, that is, changing from 0.20 to 0.17. In estimating the reliability of this index, we found that, including the shift, the value 0.20 is now clearly too large and 0.14 too small, so that we estimate $\tau \approx \tau_0 M^p$, $p = 0.17 \pm 0.03$. Not surprisingly, there is less certainty in the exponent associated with the small shift, in that $M^{0.5}$ is too strong a dependence and $M^{0.01}$ is too weak a dependence. The essential point to retain from this discussion is that the "scaling" variable provides an excellent empirical collapse of the data for viscosity ratios occurring in real reservoirs, for $M = 3$ to 300 with a value of the relaxation time index $p = 0.17 \pm 0.03$, so that

$$\langle x \rangle / t^{1.4} = f(u)$$

$$u = \{t + (8/M^{0.17})\}/M^{0.17}, \tag{8}$$

where $f(u)$ is the function shown in Figure 10. The value of the shift exponent and the actual form of the shift have no effect on later results, but only serve to improve the data collapse. It seems likely that other forms for the shift could also provide a convincing data collapse, but since the shift must be relatively small given the data, it is impossible that a different shift could effect a significant change in p, since that dependence is dominated by long-time behavior.

The dependence of front velocity upon the viscosity ratio can now be determined in a straightforward manner. Since all flows become compact for finite viscosity ratio in the limit of large times, $\langle x \rangle / t \to v(M)$. Obviously, $\langle x \rangle / t^{1+\epsilon} \to v(M) t^{-\epsilon}$; with Eq. 8 this implies that $f(u) \to v_0 u^{-\epsilon}$, since $u \to t/M^p$. Empirically from Figure 10, all the viscosity-ratio dependence is in u, not in the functional form of f. Therefore,

$$\langle x \rangle / t^{1+\epsilon} = f(u) \to v_0 u^{-\epsilon} = v_0 (M^p/t)^{\epsilon},$$

so that

$$v(M) = v_0 M^{p\epsilon}, \tag{9}$$

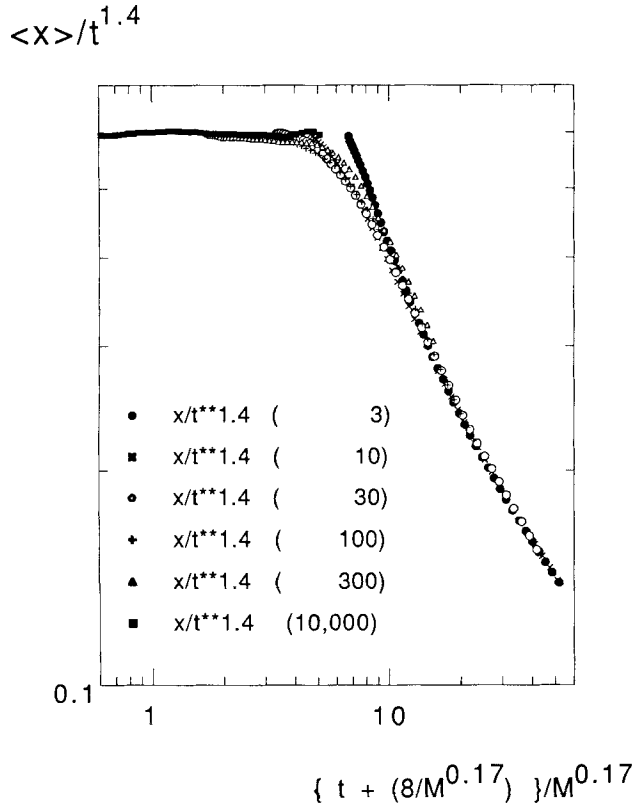

Figure 10. Scaling of $\langle x \rangle / t^{1.4}$ vs. $\{t+(8/M^{0.17})\}/M^{0.17}$.

An M-dependent shift $\Delta \approx (8/M^{0.17})$ accommodates the $t \approx 10$ deviations observed in Figure 9 with only a small change in the power of the characteristic time, now $\tau \alpha M^{0.17}$.

where $p\epsilon = 0.068 \pm 0.012$, given the value $\epsilon = 0.4$ and our determination of the relaxation time exponent, p.

Extending the fractal "scaling" of the preceding section to finite viscosity ratio shows that the factor $v(M)$ occurs in the fractional flow curves as a Koval-type factor (Koval, 1963) for long times (after the flow has become compact). In this long-time limit, we can ignore the time shift Δ, so that the finite viscosity crossover variable becomes $u \rightarrow t/M^p$. The logical form for the saturation that obeys both the scaling forms discussed separately in this and the preceding section is

$$S(x, t, M) = t^{-\epsilon} s\left(\frac{x}{t^{1+\epsilon}}, \frac{t}{M^p}\right). \tag{10}$$

Using arguments similar to those in Appendix A, one can show that this is a general form that satisfies Eq. 6. Since the flow becomes compact at long enough times, $t \gg \tau$ (that is, large $u = t/M^p$),

$$S(x, t, M) \rightarrow A\zeta\left(b\frac{x}{t}\right). \tag{11}$$

Therefore for large u, when the flow is compact,

$$t^{-\epsilon} s\left(w = \frac{x}{t^{1+\epsilon}}, u = \frac{t}{M^p}\right) \rightarrow A\zeta\left(b\frac{x}{t}\right). \tag{12}$$

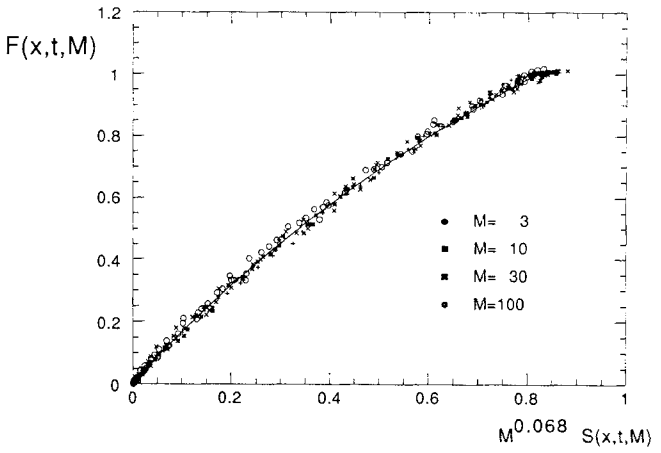

Figure 11. Koval-like form of the fractional flow from "fractal scaling."

Determined from 2-D simulations using the same definitions as in Figures 3 and 4 taken from late times (post-crossover for the viscosity ratios), this supports the reliability of the "fractal scaling" expression in Eq. 14.

The only way that Eq. 12 can be satisfied (that is, the only way that the righthand side of Eq. 12 can be written in terms of the scaling variables u and w) is for the factors of t^{ϵ} on the lefthand side to be canceled by factors of $u^{-\epsilon}$. That is,

$$t^{-\epsilon} s\left(w = \frac{x}{t^{1+\epsilon}}, u = \frac{t}{M^p}\right) \rightarrow (t^{-\epsilon})(u^{\epsilon})\zeta\left(\frac{x}{t^{1+\epsilon}}u^{\epsilon}\right)$$

$$= M^{-p\epsilon}\zeta\left(\frac{x}{M^{p\epsilon}t}\right). \tag{13}$$

Therefore, the saturation is decreased by the factor $M^{p\epsilon}$ so that in the fractional flow the saturation S must be increased by the factor $M^{p\epsilon}$. Hence, the t^{ϵ} in Eq. 4 is replaced by $M^{p\epsilon}$, giving

$$F_f = F(M^{p\epsilon}S). \tag{14}$$

This expression is verified in Figure 11, which shows the dependence of the fractional flow from our simulation in the linear regime, that is, for times well after crossover. As described in the preceding section, fractional flows and saturations were determined from our simulations for a variety of viscosity ratios. These data agree quite well with the predictions of "fractal scaling" (Eq. 14), supporting our conjecture that the fractal-to-compact crossover provides a fundamental understanding of the empirical Koval expression for the dependence of a fractional flow upon saturation and viscosity ratio in the linear-flow regime. The solid line represents a least-squares, Koval-like fit of

$$F(u) = \frac{1.74u}{1+0.517u},$$

where $u = M^{p\epsilon}S$, to the data. This fit deviates from the Koval form in that the Koval form constrains the fractional flow to become unity only for total saturation ($S = 1$) (Koval, 1963).

However, this fit to our data indicates that the fractional flow becomes unity when the saturation is less than one, that is, when $S \approx 0.82/M^{p\epsilon}$.

Conclusions

If the viscous fingering in realizable unstable two-phase flow is fractal, our general results from the second section and Appendix A show that the traditional use of composition-dependent mobilities is wrong. The mobilities, relative permeabilities, and fractional flows all depend on time as well as saturation through the variable $t^{\epsilon}S$. These general results compared successfully with saturation profiles and fractional flows generated from simulations for our fractal model.

In the context of our specific model of Poiseuille flow (infinite capillary number) in homogeneous, two-dimensional model porous media, our results for finite viscosity ratios from the preceding section show that initial fractal flows relax to compact [linear $\langle x \rangle = v(M)t$] flow on a characteristic time scale, τ. Scaling arguments were used to analyze the data, enabling an empirical determination of the viscosity-ratio dependence of the crossover time, $\tau \approx \tau_0 M^p$ ($p = 0.17 \pm 0.03$), and the front velocity, $v(M) = v_0 M^{p\epsilon}$ ($p\epsilon = 0.068 \pm 0.012$). These scaling arguments also showed that the front velocity $v(M)$ acted as a 2-D Koval factor in scaling the saturation dependence of the postcrossover fractional flow.

Our results for the values of the exponents p and ϵ are for strictly two-dimensional porous media; in comparing our two-dimensional results with experiment, one must take care that the experiments are truly two-dimensional. Even the seemingly 2-D experiments of Blackwell (1959) have enough thickness to be nearly three-dimensional, if the crossover occurs on a short enough length scale in three dimensions. Blackwell's cells had a 3/8-in. (95-mm) thickness of 60–80-mesh sand (sand-grain diameter of less than 0.25 mm) so that more than 40 sand grains fit across the 3/8-in. (95-mm) thickness cell (Blackwell et al., 1959). If our porous media were $60 \times 300 \times 40$, they would be clearly three-dimensional, suggesting that Blackwell's cells are too thick to warrant comparison with our 2-D results.

Therefore, our modeling of 2-D floods in homogeneous reservoirs provides evidence that finite viscosity-ratio flow becomes compact on a reasonable time scale, so that one might assume that the difficulties associated with fractal flow need not be a real concern. However, although we have adapted common pore-level models for simulating two-phase flow and although we have endeavored to make our model as physically rigorous as possible, it is not known how modifications of the model might affect our results for the fractal-to-compact crossover. Extending our model to three dimensions might not qualitatively change the crossover, but it would certainly give different power-law dependencies for the characteristic time and "front" velocity, v. On the other hand, heterogeneities in the reservoir might serve to stabilize the fractal nature of the flow, delaying or even preventing the crossover. Furthermore, it seems likely that for finite capillary number, the capillary pressure would help stabilize the fractal nature of the flow (Lenormand et al., 1988).

Therefore, the significance of the conclusions (fractal flow radically alters traditional assumptions) is not rendered useless by the conclusions of the preceding section (the fractal-to-compact crossover in our model flows), because, first, our derivation of the effects of fractal flow are model independent and quite general, while the fractal-to-compact crossover is model specific. Furthermore, even if the fractal-to-compact crossover proves to be a general effect, the "fractal scaling" of the saturation and fractional flow associated with this crossover provides a fundamental understanding of the empirical Koval factor.

Acknowledgments

M. F. gratefully acknowledges the support of the Fossil Energy Program, U.S. Dept. of Energy, partly through his appointment to the Part-Time Faculty Research Participation Program administered by Oak Ridge Associated Universities. This work was initiated while M. F. held a National Research Council–U.S. DOE Senior Research Associateship.

Notation

A = cross-sectional area of porous medium
D_f = fractal dimension, specifying non-Euclidean relationship between mass and size
F = fractional flow of injected fluid
M = viscosity ratio
N_x = number of pore bodies along the length ($\parallel$ flow) of our model porous medium
N_y = number of pore bodies along the width ($\perp$ flow) of our model porous medium
P = pressure
q = flow rate
r = pore throat radius
$\mathfrak{R}$ = residual in Gauss-Seidel scheme
S = saturation of injected fluid
t = dimensionless time $\equiv$ total saturation
T = pore throat conductance $\equiv$ pore throat transmissibility
v = front velocity
$\langle x \rangle$ = first moment of the saturation, related to the position of the front

Greek letters

ϵ = index relating front position and time for fractal flow, $1 + \epsilon = 1/(D_f - 1)$
ϕ = porosity
μ = viscosity
τ = characteristic time for fractal-to-compact crossover

Literature Cited

Blackwell, R. J., J. R. Rayne, and W. M. Terry, "Factors Influencing the Efficiency of Miscible Displacement," *Trans. AIME*, **216**, 1 (1959).

Buckley, S. E., and M. C. Leverett, "Mechanism of Fluid Displacement in Sands," *Trans. AIME*, **146**, 107 (1942).

Chen, J.-D., and D. Wilkinson, "Pore-Scale Viscous Fingering in Porous Media," *Phys. Rev. Lett.*, **55**, 1892 (1985).

Collins, R. E., *Flow of Fluids through Porous Materials*, Reinhold, New York (1961).

Daccord, G., J. Nittmann, and H. E. Stanley, *Fractal Viscous Fingers: Experimental Results. On Growth and Form*, Nijhoff, Dordrecht, The Netherlands (1986).

de Gennes, P. G., *Scaling Concepts in Polymer Physics*, Cornell Univ. Press, Ithaca, NY (1979).

Fatt, I., "The Network Model of Porous Media," *Trans. AIME*, **207**, 144 (1956).

Feder, J., *Fractals*, Plenum, New York (1988).

Ferer, M., W. N. Sams, R. A. Geisbrecht, and D. H. Smith, "Crossover from Fractal to Compact Growth from Simulations of Two Phase Flow with Finite Viscosity Ratio in Two-Dimensional Porous Media: Linear Flow," *Phys. Rev. E*, **47**, 2713 (1993).

Ferer, M., R. A. Geisbrecht, W. N. Sams, and D. H. Smith, "Crossover from Fractal to Compact Growth from Simulations of Two Phase Flow with Finite Viscosity Ratio in Two-Dimensional Porous Media: Radial Flow," *Phys. Rev. A*, **45**, 6973 (1992).
Fisher, M. E., "The Theory of Equilibrium Critical Phenomena," *Rep. Progr. Phys.*, **30**, 615 (1967).
Kadanoff, L. P., et al., "Static Phenomena Near Critical Points: Theory and Experiment," *Rev. Mod. Phys.*, **39**, 395 (1967).
King, P. R., "The Fractal Nature of Viscous Fingering in Porous Media," *J. Phys. A.*, **20**, L529 (1987).
Koval, E. J., "A Method of Predicting the Performance of Unstable Miscible Displacement in Heterogeneous Media," *Soc. Pet. Eng. J.—Trans. AIME*, **228**, 145 (1963).
Lenormand, R., E. Touboul, and C. Zarcone, "Numerical Models and Experiments on Immiscible Displacements in Porous Media," *J. Fluid Mech.*, **189**, 165 (1988).
Maloy, K. J., J. Feder, and T. Jossang, "Viscous Fingering Fractals in Porous Media," *Phys. Rev. Lett.*, **55**, 2688 (1985).
Mandelbrot, B. B., *The Fractal Geometry of Nature*, Freeman, New York (1982).
Meakin, P., "Diffusion Controlled Cluster Formation in Two, Three, and Four Dimensions," *Phys. Rev. A*, **27**, 604 (1983a).
Meakin, P., "Diffusion Controlled Deposition on Fibers and Surfaces," *Phys. Rev. A*, **27**, 2616 (1983b).
Nittmann, J., G. Daccord, and H. E. Stanley, "Fractal Growth of Viscous Fingers: Quantitative Characterization of a Fluid Instability Phenomenon," *Nature*, **314**, 141 (1985).
Peaceman, D. W., *Fundamentals of Numerical Reservoir Simulation. Developments in Petroleum Science*, Elsevier, Amsterdam (1977).
Rhee, H.-K., R. Aris, and N. R. Amundson, *First-Order Partial Differential Equations*, Vol. 1, *Theory and Applications of Single Equations*, Prentice-Hall, Englewood Cliffs, NJ (1986).
Saffman, P. G., and G. I. Taylor, "The Penetration of a Fluid into a Medium or Hele-Shaw Cell Containing a More Viscous Liquid," *Proc. Roy. Soc. London*, **A245**, 312 (1958).
Siddiqui, H., and M. Sahimi, "Computer Simulations of Miscible Displacement Processes in Disordered Porous Media," *Chem. Eng. Sci.*, **45**, 163 (1990).
Stauffer, D. S., *Introduction to Percolation Theory*, Taylor & Francis, (1985).
Thomas, G. W., *Principles of Hydrocarbon Reservoir Simulation*, International Human Resources Development Corp., Boston (1982).
Tobin, T., R. Muralidhar, H. Wright, and D. Ramkrishna, "Determination of Coalescence Frequencies in Liquid-Liquid Dispersions: Effect of Drop Size Dependencies," *Chem. Eng. Sci.*, **45**, 3491 (1990).
van Dongen, P. G. J., and M. H. Ernst, "Kinetics of Reversible Polymerization," *J. Stat. Phys.*, **37**, 301 (1984).
van Dongen, P. G. J., and M. H. Ernst, "Cluster Size Distribution in Irreversible Aggregation at Large Times," *J. Phys. A*, **18**, 2779 (1985).
Vicsek, T., *Fractal Growth Phenomena*, World Scientific, Singapore (1989).
Witten, T. A. J., and L. M. Sander, "Diffusion Limited Aggregation, A Kinetic Critical Phenomenon," *Phys. Rev. Lett.*, **47**, 1400 (1981).

Appendix A: Detailed Derivation of the Fractal Scaling Form for the Saturation

The average position of the saturation (Ferer et al., 1993) is defined as

$$\langle x\rangle = \int_{x=0}^{L} xS(x,t)\,dx \Big/ \int_{x=0}^{L} S(x,t)\,dx, \tag{A1}$$

where the denominator is simply the total saturation that is proportional to the time and will be used to define a dimensionless time, so that

$$t \equiv \int_{x=0}^{L} S(x,t)\,dx. \tag{A2}$$

We have found it difficult to adhere strictly to the standard % pore-volume normalization of saturation because of the nonlinearity of fractal flow and because of our use of different sizes of systems. We therefore specify our normalization of saturation as needed. For fractal flow, the average position is known to grow faster than linearly

$$\langle x\rangle = At^{1+\epsilon}, \tag{A3}$$

where $\epsilon = 0.4$ in our case (see the third section) (Meakin, 1983a). From these equations, we show that the saturation should have the functional form

$$S(x,t) = t^{-\epsilon} s(x/t^{1+\epsilon}). \tag{A4}$$

We also show that conservation of our incompressible fluids requires that the fractional flow be a function not simply of the saturation but rather of $t^{\epsilon}S$.

For fractal flow the average position is known to grow faster than linearly as $t^{1+\epsilon}$, Eq. A3. Therefore, if time is doubled, that is, $t \to 2t$ (more generally $t \to \lambda t$), the average position grows faster than linearly by an extra factor of 2^{ϵ} (more generally λ^{ϵ}). In the familiar case where the front advances linearly with t, the saturation is a function of x/t, so that doubling both x and t gives the same saturation. That is, if $S(x, t) = \zeta(x/t)$, then $S(2x, 2t) = \zeta(x/t) = S(x, t)$, which is consistent with linear advance of the front. In our fractal case, the front advances as $t^{1+\epsilon}$, so that the saturation must be a function of $x/t^{1+\epsilon}$, so that all the x-dependence in the saturation must be associated with a factor of $1/t^{1+\epsilon}$. However, there may be additional, separate t-dependence in the saturation, so that $S(x, t) = G(t)g(x/t^{1+\epsilon})$. We now show that Eqs. A1 and A2 together determine the form of this additional t-dependence and require the conjectured $x/t^{1+\epsilon}$ dependence. Using the conjectured form for the saturation profile in Eq. A2 gives

$$t \equiv G(t)\int_{x=0}^{L} g(x/t^{1+\epsilon})\,dx = t^{1+\epsilon}G(t)\int_{u=0}^{u_{\max}} g(u)\,du, \tag{A5}$$

where $u = x/t^{1+\epsilon}$, and before breakthrough the integrand is zero at the upper limits, so that the values of the upper limits do not affect the value of the integral. Normalizing $g(u)$,

$$\int_{u=0}^{u_{\max}} g(u)\,du = 1,$$

implies $G(t) = t^{-\epsilon}$. Therefore, the saturation profile conjectured in Eq. A4 obeys Eq. A2. This conjectured form also satisfies the fractal "scaling" of the average position, that is,

$$\langle x\rangle = \frac{\int_{x=0}^{L} xt^{-\epsilon}s(x/t^{1+\epsilon})\,dx}{\int_{x=0}^{L} t^{-\epsilon}s(x/t^{1+\epsilon})\,dx} = \frac{t^{-\epsilon}\int_{u=0}^{u_{\max}} t^{1+\epsilon}us(u)t^{1+\epsilon}\,du}{t^{-\epsilon}\int_{u=0}^{u_{\max}} s(u)t^{1+\epsilon}\,du} \tag{A6}$$

so that

$$\langle x \rangle = \frac{t^{2+\epsilon}\int_{u=0}^{u_{\max}} u g(u)\, du}{t} = A t^{1+\epsilon}.$$

If one chooses the most general such scaling form, that is, $S(x, t) = G(t)\, g(x/f(t))$ the preceding arguments would show that one must have $f(t) = t^{1+\epsilon}$ and $G(t) = t^{-\epsilon}$. Therefore, we have shown that the standard definition of time as total saturation (Eq. A2) and the fractal scaling of the average position (Eq. A3) lead to the scaling of the saturation shown in Eq. A5 and discussed in the text.

Now, we will show that conservation of our incompressible fluids requires that the fractional flow of injected fluid F_I depends not simply on the saturation of injected fluid S, but rather on the time-dependent variable $t^{\epsilon}S$. Writing the continuity equation for the incompressible injected fluid, we have

$$\frac{\partial F_I(x, t')}{\partial x} = -\left(\frac{\phi A}{q}\right)\frac{\partial S_I(x, t')}{\partial t'}, \tag{A7}$$

where t' is ordinary time and where the porosity ϕ, cross-sectional area A, and total flow rate q are all constant. Since the ratio $\phi A/q$ is a constant, it can be used to define a new unit of time, so that in this unit, time is equal to $t = t'/(\phi A/q)$. This enables us to write Eq. A7 in the simplified form

$$\frac{\partial F_I(x, t)}{\partial x} = -\frac{\partial S_I(x, t)}{\partial t}. \tag{A8}$$

Using the scaling form Eq. A4 for the saturation in Eq. A8, and differentiating one finds

$$\begin{aligned}\frac{\partial F_I(x, t)}{\partial x} &= -\frac{\partial t^{-\epsilon} s(x/t^{1+\epsilon})}{\partial t} \\ &= -\left\{\frac{-\epsilon}{t^{1+\epsilon}} s(u) + t^{-\epsilon}\frac{du}{dt}\frac{ds(u)}{du}\right\} \\ &= -\frac{1}{t^{1+\epsilon}}\left\{-\epsilon s(u) - (1+\epsilon)u\frac{ds(u)}{du}\right\},\end{aligned} \tag{A9}$$

where $u = x/t^{1+\epsilon}$. Multiplying through by $t^{1+\epsilon}$ enables us to rewrite Eq. A9 as

$$\frac{\partial f_I(x, t)}{\partial u} = \mathfrak{F}'(u) \tag{A10}$$

where $\mathfrak{F}'(u) = \epsilon s(u) + (1+\epsilon)u\,\dfrac{ds(u)}{du}$. Integrating Eq. A10 yields

$$F_I(x, t) = \mathfrak{F}\left(\frac{x}{t^{1+\epsilon}}\right). \tag{A11}$$

Since $s(u)$ should be a monotonic function of u, one can invert Eq. A4 to find $u \equiv x/t^{1+\epsilon} = s^{-1}(t^{\epsilon}S)$, which, when used in Eq. A11, yields

$$F_I = \mathfrak{F}\{u\} = \mathfrak{F}\{s^{-1}(t^{\epsilon}S)\} = F(t^{\epsilon}S). \tag{A12}$$

Therefore, for fractal flow (when Eq. A3 applies) the usual assumption of relative permeabilities and fractional flows that depend only upon saturation is fundamentally incorrect.

Appendix B: Description of the Model

In modeling two-dimensional porous media, we have used a variant of a standard square lattice representation (Fatt, 1956; Chen and Wilkinson, 1985; Siddiqui and Sahimi, 1990; King, 1987). This $N_x \times N_y$ square lattice model has pore bodies of unit volume at the lattice sites, $\vec{r} = (2m, 2n)$ for all integers $m = 1 \rightarrow N_x$ and $n = 1 \rightarrow N_y$. These pore bodies are connected by cylindrical throats of unit length at the vertical and horizontal bond locations, $\vec{r} = (2m+1, 2n)$ and $(2m, 2n+1)$, respectively. The randomly chosen cross-sectional areas of these throats are uniformly distributed in the interval 0 to 1. This assures that the conductances (transmissibilities) are randomly distributed so that the growth will be random rather than dendritic (Chen and Wilkinson, 1985). Furthermore, the finite volume of the throats allows for realistically smooth variations in the conductance of a throat as it becomes invaded, which is not the case in models where a zero-volume throat is either occupied or unoccupied (Chen and Wilkinson, 1985; King, 1987).

To ascertain the effects of a finite viscosity ratio, we assume Poiseuille flow through a throat, neglecting the surface tension effects, capillary pressure, and wetting. Poiseuille's law relates the pressure drop (ΔP) across a throat and the volume flow rate (q) through that throat, for example, for the throat at $\vec{r} = (2m+1, 2n)$

$$\begin{aligned}\Delta P_{2m+1,2n} &= q_{2m+1,2n}/T_{2m+1,2n}, \\ P_{2m,2n} - P_{2m+2,2n} &= \left\{\frac{\mu_I x_{2m+1,2n} + \mu_D(1 - x_{2m+1,2n})}{C r^4_{2m+1,2n}}\right\} q_{2m+1,2n}\end{aligned} \tag{B1}$$

where T is the transmissibility (or conductance) of the throat, x is the length (fraction of the unit length) of throat invaded, and r is the radius of this throat, and where C is a constant. Imposing the condition that the net volume flow into any pore body must be zero, for example, for the pore body at $(2m, 2n)$

$$q_{2m+1,2n} + q_{2m,2n+1} + q_{2m-1,2n} + q_{2m,2n-1} = 0, \tag{B2}$$

which is equivalent to volume conservation for our incompressible fluids. Using Poiseuille's law, Eq. B1 in this conservation equation, one finds a discretized Laplace's equation:

$$P_{2m,2n} = \frac{T_{2m+1,2n}P_{2m+2,2n} + T_{2m,2n+1}P_{2m,2n+2} + T_{2m-1,2n}P_{2m-2,2n} + T_{2m,2n-1}P_{2m,2n-2}}{T_{2m+1,2n} + T_{2m,2n+1} + T_{2m-1,2n} + T_{2m,2n-1}}, \tag{B3}$$

where we have chosen boundary conditions with a high pressure at the inlet pore bodies at $x = 0$ ($P_{0,2n} = 100$); zero pressure at the outlet edge at ($P_{2N_x+2,2n} = 0$); and no flow conditions imposed on the sides ($T_{2m,1} = T_{2m,2N_y+1} = 0$). To find iterative solutions for the pressure field, we have used a slight variant of the standard overrelaxed Gauss-Seidel scheme (Peaceman, 1977) such that the normalized residuals $\mathcal{R}$,

$$\mathcal{R} = \sum \left\{ \frac{q_{2m+1,2n} + q_{2m,2n+1} + q_{2m-1,2n} + q_{2m,2n-1}}{T_{2m+1,2n} + T_{2m,2n+1} + T_{2m-1,2n} + T_{2m,2n+1}} \right\}^2, \tag{B4}$$

fall below a confidence limit that we have normally chosen to be 10^{-5} or 10^{-6}. These confidence limits plus the flow rules described below satisfy overall fluid conservation to within a fraction of 1% (we find differences that are typically less than 0.5% when we compare the total volume of invading fluid in the porous medium up to breakthrough with the volume of displaced fluid).

Having (1) defined the porous medium, (2) determined the transmissibilities, (3) solved for the initial pressure field iteratively, and (4) found the initial volume flows in the pore throats, we can now advance the interface through some short time interval Δt. We have chosen a Δt such that the interface advances one-half pore body volume (that is, one-half unit) in that interface throat with the maximum volume flow rate: $Q_{\max}\Delta t = 1/2$. The flow rules allow the interface to advance through throats such that the flow is from a fully invaded pore-body toward a pore body that is not yet fully invaded. As shown in Figure B1a, this advance can occur within the pore throat, into the pore body, or through the pore body into the adjacent outflow throats. These flow rules also allow the interface to retreat locally through throats where the flow is from a pore body that is not fully invaded toward a pore body that is fully invaded (or was fully invaded and is not yet completely defender filled). As shown in Figure B1b, this retreat can occur within the pore throat, into a fully invaded pore body, or even through a pore body into the outflow throats.

We then cycle this process: (1) find the transmissibilities for the new interface location, (2) solve for the new pressure field, (3) determine the new volume flow rates, and (4) advance the interface through $\Delta t = 1/(2q_{\max})$ until "breakthrough" when the interface reaches the edge of the porous medium. The largest models that we have used consist of $90 \times 300 = 27{,}000$ pore bodies; for these largest systems to reach breakthrough, we find that we must cycle this process from as few as 700 times to as many as 1,400 times, depending on the viscosity ratio and on the individual porous medium. The longest of these runs used 21 hours of CPU time on an FPS vector array processor.

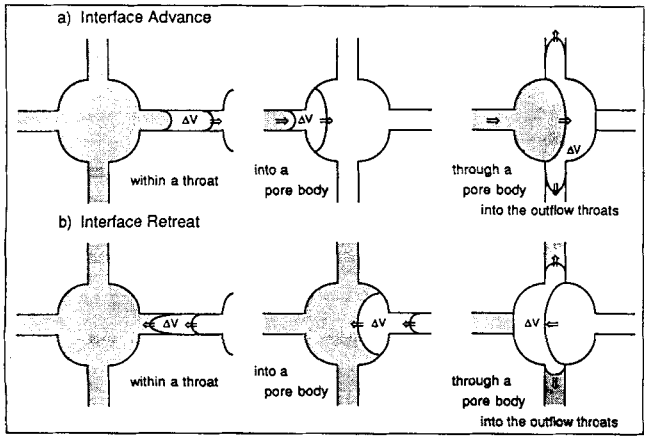

Figure B1. Flow rules in the model.

The flow can cause the interface (a) to advance through a volume $\Delta V = u\Delta t$ within a pore throat, from the pore throat into the connected pore body, and from the pore body into the outflow throats; (b) to retreat through a volume $\Delta V = u\Delta t$ within a pore throat, from the pore throat into the connected pore body, and from the pore body into the outflow throats.

Appendix C: Effect of Lattice Discreteness on the Average Interface Position

For a large (macroscopic) system, one expects that when even a few percent of a pore volume has been injected the discreteness of the medium will not affect observations. In a continuum model we can define the average position of the mass of injected fluid as

$$\langle x \rangle = \int_{x=0}^{L} x[S(x)/S_{\text{tot}}]\, dx, \tag{C1a}$$

$$S_{\text{tot}} = \int_{x=0}^{L} S(x)\, dx, \tag{C1b}$$

where $S(x)$ is the saturation profile from $x = 0 \rightarrow L$ (Ferer et al., 1993). However, in our discrete $N_x \times N_y$ square lattice models of length L_x and width L_y, one does not have a continuous saturation profile, but rather one has a saturation for each row of lattice sites: that is, $s(i)$ for the ith row, $i = 1 \rightarrow N_x$. Therefore, the average position will be given by the sum

$$\langle x \rangle = \sum_{i=1}^{N_x} ia[s(i)/S_{\text{tot}}], \tag{C2a}$$

where

$$S_{\text{tot}} = \sum_{i=1}^{N_x} s(i), \tag{C2b}$$

and where the rows of the lattice are a distance $a = L_x/N_x$ apart. At this point, we choose our length scale so that $a \equiv 1$, which makes both sums and integrals dimensionless and which enables us to treat the integrand and summand interchangeably: $s(i) = S(x = i)$. For a very large system ($L \gg 1$), the discreteness of our model is unobservable on a scale of the system size, and the sums in Eqs. C2 approach the corresponding integrals in Eqs. C1 in the usual way.

However, for small values of $\langle x \rangle$, the discreteness of our lattice model does affect the relationship between $\langle x \rangle$ and S_{tot}. Fortunately, quantifying this effect for compact (nonfractal) flow enables us to define an effective saturation that

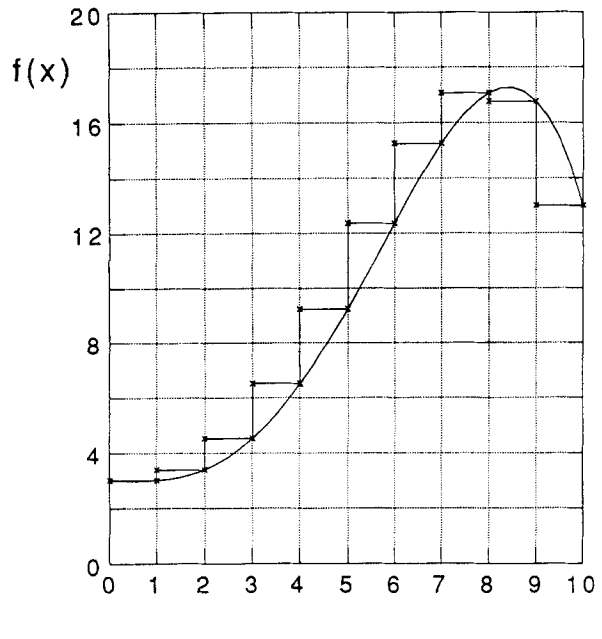

Figure C1. Smooth curve shows the function $f(x)=3.0-0.15x^2+0.18x^3-0.0225x^4$.

The area under the histogram gives the value of the sum in Eq. C4.

minimizes these small $\langle x\rangle$ deviations. To understand the genesis of this effective saturation, we first consider the difference between the sums (Eqs. C2) and the integrals (Eqs. C1). For a typical function, for example, $f(x)=3.0-0.15x^2+0.18x^3-0.0225x^4$, which is the smooth curve shown in Figure C1, the integral

$$\text{Integral}=\int_{x=0}^{10} f(x)\,dx \tag{C3}$$

is equal to the area under the smooth curve, while the sum

$$\text{Sum}=\sum_{i=1}^{10} f(i)=f(1)+f(2)+f(3)+\cdots+f(9)+f(10) \tag{C4}$$

equals the area under the histogram shown in Figure C1. Clearly, the integral would be better approximated by the area under a trapezoidally segmented curve than by the area under this histogram, Eq. C4, that is,

$$\text{Integral}\approx\frac{f(0)+f(1)}{2}+\frac{f(1)+f(2)}{2}+\frac{f(2)+f(3)}{2}+\frac{f(3)+f(4)}{2}+\cdots+\frac{f(8)+f(9)}{2}+\frac{f(9)+f(10)}{2}. \tag{C5}$$

The difference between the estimates in Eqs. C5 and C4 (between the sum and the trapezoidal estimate) is equal to the area of the triangular portions above the curve (Figure C1) from $x=0\rightarrow 8$ minus the area of the triangular portions below the curve from $x=8\rightarrow 10$, that is, Eq. C4 minus Eq. C5 is simply

$$\text{Sum}-\text{Integral}\approx\frac{f(10)-f(0)}{2}. \tag{C6}$$

The form of effective saturation that minimizes discreteness effects is most easily derived for pistonlike displacement. Consider the pistonlike motion of an interface through $i=l$; for our $N_x\times N_y$ rectangular lattice, the saturation of a row of pore bodies is N_y, for all rows through the flat-interface between $i=l$ and $l+1$, where 1 is the single pore body saturation. For this case, the total saturation is the same in both the continuum ($S_{\text{tot},c}=$ integral Eq. C1b) and discrete ($S_{\text{tot},D}=$ sum Eq. C2b) cases, being the area of a rectangle of height N_y and base l,

$$S_{\text{tot},I}=S_{\text{tot},D}=lN_y \tag{C7}$$

since the difference in Eq. C6 is zero [here, $f(l)=f(0)$]. However, the results for the average $\langle x\rangle$ differ. From the integral that evaluates the area of a triangle of height lN_y and base l, we have

$$\langle x\rangle_c=\frac{1}{S_{tot}}(lN_y)\left(\frac{l}{2}\right)=\left(\frac{l}{2}\right). \tag{C8}$$

Equation C6 shows us that the sum will give the result

$$\langle x\rangle_D=\frac{1}{S_{\text{tot}}}\left\{(lN_y)\left(\frac{l}{2}\right)+\frac{1}{2}[(lN_y)-0]\right\}=\frac{l+1}{2}, \tag{C9}$$

where the first term in the curly bracket results from the integral in Eq. C8 and the second term results from the excess of Eq. C6. Therefore, the linear behavior of Eq. C8, resulting from a continuum model

$$\langle x\rangle_C=\left(\frac{l}{2}\right)=\frac{1}{2}\,\frac{S_{\text{tot}}}{N_y} \tag{C10}$$

is mimicked for the discrete model

$$\langle x\rangle_D=\left(\frac{l+1}{2}\right)=\frac{1}{2}\left\{\frac{S_{\text{tot}}+1}{N_y}\right\} \tag{C11}$$

if one uses $S_{\text{eff}}\equiv t_{\text{eff}}N_y\equiv S_{\text{tot},D}+N_y$ as an effective saturation variable in the discrete model. This defines effective time used in the analysis of the moments.

Surprisingly, it is possible to verify that this same effective saturation applies for general compact (nonfractal) flow. In this case, where one can write $S(x,t)=S(x/t)$, evaluating the integrals (Eqs. C1) for total saturation and average position both yield results proportional to t

$$S_{\text{tot},C}=aN_yt \tag{C12}$$

$$\langle x\rangle_C=bt \tag{C13}$$

so that the average position is proportional to total saturation

$$\langle x\rangle_C = \frac{b}{a}\,\frac{S_{\mathrm{tot},C}}{N_y}. \tag{C14}$$

If one has a smooth saturation profile $S(x/t)$ varying from $S(0)=N_y$ to $S(x/t)=0$ for $x/t \geq v$, Eq. C6 shows that the discrete evaluation of the total saturation is given by

$$S_{\mathrm{tot},D} \approx S_{\mathrm{tot},C} + \frac{1}{2}(0-N_y) = at - \frac{1}{2}N_y, \tag{C15}$$

while the discrete evaluation of the unnormalized moment gives the same result as the integral

$$S_{\mathrm{tot},D}\langle x\rangle_D \approx S_{\mathrm{tot},C}\langle x\rangle_C + \frac{1}{2}(0-0) = (aN_y t)(bt), \tag{C16}$$

since the integrand $xS(x)$ is zero at both limits of integration. Using Eq. C15 to replace $(aN_y t)$ by $S_{\mathrm{tot},D} + \frac{1}{2}N_y$ in Eq. C16, one finds

$$\langle x\rangle_D \approx \frac{b}{aN_y}\,\frac{\left(S_{\mathrm{tot},D}+\frac{1}{2}N_y\right)^2}{S_{\mathrm{tot},D}} \approx \frac{b}{aN_y}\{S_{\mathrm{tot},D}=N_y\}, \tag{C17}$$

where we neglect the quadratic term $\{\frac{1}{2}N_y\}^2/S_{\mathrm{tot},D}$ because it is of order t^{-1}, whereas the two terms retained are of order t^{+1} and t^0. In Eq. C17, note that this is simply our definition of effective saturation

$$t_{\mathrm{eff}} \equiv \left\{\frac{S_{\mathrm{tot},D}}{N_y}+1\right\} \tag{C18}$$

so that

$$\langle x\rangle_C = \frac{b}{a}t_{\mathrm{eff}}. \tag{C19}$$

This provides a first-order correction to the difference between continuous and discrete determinations. Therefore, use of this effective saturation (or effective time) enables us to reduce the small time and distance effects of discreteness upon the relation between the average position and the saturation.

If the relationship is fractal, one can proceed in a similar fashion realizing that the equation for the average position from the continuous evaluation in Eq. C13 becomes

$$\langle x\rangle_C = bt^{1+\epsilon},$$

while the equation for the total saturation in Eq. C12 as well as the relations between the discrete and continuous evaluations, Eqs. C15 and C16, remain unchanged. Replacing the (bt) by $(bt^{1+\epsilon})$ in Eq. C16 and using Eq. C15 to replace $(aN_y t)$ by $S_{\mathrm{tot},D}+(1/2)N_y$, one finds

$$\langle x\rangle_D \approx \frac{b}{aN_y}\,\frac{\left(S_{\mathrm{tot},D}+\frac{1}{2}N_y\right)^{2+\epsilon}}{S_{\mathrm{tot},D}}. \tag{C20}$$

Assuming that $t_{\mathrm{eff}} = (S_{\mathrm{tot},D}/N_y)+c$, the undetermined constant c can be determined by requiring that the correction to first order in $1/t_{\mathrm{eff}}$ vanishes; that is, using this definition of t_{eff} in Eq. C20 one finds

$$\langle x\rangle_D \approx \frac{bN_y^{\epsilon}}{a}\,\frac{\left(t_{\mathrm{eff}}-c+\frac{1}{2}\right)^{2+\epsilon}}{t_{\mathrm{eff}}-c}$$

$$= \frac{bN_y^{\epsilon}}{a}\,t_{\mathrm{eff}}^{1+\epsilon}\,\frac{\left\{1-t_{\mathrm{eff}}^{-1}\left(c-\frac{1}{2}\right)\right\}^{2+\epsilon}}{1-t_{\mathrm{eff}}^{-1}c}. \tag{C21}$$

Expanding in powers of t_{eff}^{-1}, we find

$$\langle x\rangle_D \approx \frac{bN_y^{\epsilon}}{a}t_{\mathrm{eff}}^{1+\epsilon}\left\{1+t_{\mathrm{eff}}^{-1}\left\{-(2+\epsilon)\left(c-\frac{1}{2}\right)+c\right\}+O(t_{\mathrm{eff}}^{-2})\right\}. \tag{C22}$$

Requiring that the coefficient of t_{eff}^{-1} be zero determines the value of c, in t_{eff}

$$t_{\mathrm{eff}} = \frac{S_{\mathrm{tot},D}}{N_y} + \frac{1}{2}\,\frac{2+\epsilon}{1+\epsilon}. \tag{C23}$$

Therefore, use of this effective time in a discrete model accounts for the difference between sums and integrals through first order in t_{eff}^{-1}.

For the actual model discussed in the article and in Appendix B, there are N_y throats parallel to the x-axis at $x = 2m+1$ containing a total volume $(1/2)N_y$, as well as pore bodies and throats parallel to the y-axis at $x=2m$ containing a total volume $(3/2)N_y$. When one reproduces the piston-like discussion for this model, one finds for compact flow $t_{\mathrm{eff}} = (S_{\mathrm{tot},D}/N_y)+1.5$, while for fractal flow, where $\epsilon = 0.4$, $t_{\mathrm{eff}} = (S_{\mathrm{tot},D}/N_y)+1.2$. The latter definition with the additive factor of 1.2 was used in the analysis to reduce the early time curvature due to the difference between discrete and continuous models.

Manuscript received Oct. 6, 1993, and revision received May 5, 1994.